



High Photoluminescence Quantum Yield of 18.7% by Nitrogen-Doped Ti₃C₂ MXene Quantum Dots

Journal:	<i>Journal of Materials Chemistry C</i>
Manuscript ID	TC-COM-05-2018-002156.R1
Article Type:	Communication
Date Submitted by the Author:	25-May-2018
Complete List of Authors:	<p>Xu, Quan; China University of Petroleum (Beijing), Institute of New Energy Ding, Lan; North China University of Science and Technology Wen, Yangyang; China University of Petroleum Beijing, Institute of new energy Yang, Wenjing; State Key Laboratory of Heavy Oil Processing Zhou, Hongjun; China University of Petroleum Beijing Chen, Xingzhu; Wuhan University of Technology, State Key Laboratory of Silicate Materials for Architectures Street, Jason; Mississippi State University, Department of Sustainable Bioproducts Zhou, Aiguo; Henan Polytechnic University, School of Materials Science and Engineering Ong, Wee-Jun; Agency for Science Technology and Research, Institute of Materials Research and Engineering (IMRE) Li, Neng; Wuhan University of Technology, State key laboratory of silicate materials for architectures</p>

High Photoluminescence Quantum Yield of 18.7% by Nitrogen-Doped Ti₃C₂ MXene Quantum Dots

Quan Xu,^{a} Lan Ding,^a Yangyang Wen,^a Wenjing Yang,^a Hongjun Zhou,^a Xingzhu Chen,^b
Jason Street,^c Aiguo Zhou,^d Wee-Jun Ong,^e Neng Li,^{b*}*

AUTHOR ADDRESS:

- a. State Key Laboratory of Heavy Oil Processing, China University of petroleum(Beijing),
102249, China
- b. State Key Laboratory of Silicate Materials for Architectures, Wuhan University of
Technology, Hubei, 430070, China
- c. Department of Sustainable Bioproducts, Mississippi State University, 39762, USA
- d. School of Materials Science and Engineering, Henan Polytechnic University, 454003,
China
- e. Department of Chemical Engineering, Xiamen University Malaysia, Jalan Sunsuria,
Bandar Sunsuria, 43900 Sepang, Selangor Darul Ehsan, Malaysia

KEYWORDS: MXene; Two-dimensional material (2D); Quantum dots; Mechanism;
Bio-sensors

ABSTRACT: Quantum dots, derived from two-dimensional (2D) materials, have shown promising applications in bioimaging, photocatalysis, biosensors and white light emission devices (W-LEDs). Herein, this work involves producing a high photoluminescence quantum yield (PLQY) of 2D transition metal carbides MXene (nitrogen-doped, N-doped Ti_3C_2) quantum dots using Ti_3C_2 as a precursor and ethylenediamine as a nitrogen source. The hydrothermally treated N-doped Ti_3C_2 quantum dots developed in this study have an average size of 3.4 nm and a PLQY of up to 18.7%, which is by far the highest QY reported to date. The mechanism of the enhanced PLQY of N-doped Ti_3C_2 quantum dots is systematically discussed by using comprehensive spectroscopic techniques (e.g. grazing incidence X-ray diffraction (GIXRD)) and complementary density functional theory (DFT) calculations. Furthermore, the N-doped Ti_3C_2 quantum dots are applied as an ultra-sensitive heavy iron ion (Fe^{3+}) detector probe with a detection limit of up to 100 μM . Additionally, the as-developed MXene quantum dots have a huge prospect in biological sensing by functioning as an appealing mediator-free biosensor for the detection of H_2O_2 with a high sensitivity. Overall, this work will provide a blueprint for the design of 2D-QDs based on MXene toward meeting the continuous upsurge in demand for a plethora of technological applications such as electronics, solar cells, optical, biomedical, and environmental fields.

1 INTRODUCTION

MXene, a conceptually new layered material, has triggered a recent resurgence of interest because of its unique structure as well as fascinating optical and electronic properties. MXene, composed of early transition metal carbides and/or carbonitrides is generally produced by selectively etching out the A layers from $\text{M}_{n+1}\text{AX}_n$ phases, (where M is an early transition metal, A is an A-group and X is C and/or N).¹ The characteristics of MXene make it a promising candidate for energy storage,² environmental applications,³ adsorption of organic

molecules,⁴ photocatalysis,⁵⁻⁶ supercapacitors,⁷⁻⁸ electromagnetic absorption,⁹ and ion-exchange¹⁰ applications. Although MXene exhibits a great potential to be used as a biosensing device, this material generally exhibits a low photoluminescence (PL) response in an aqueous solution, which significantly limits their direct use in biological and optical applications. A bright PL response and optical absorption are essential for nanomaterials to be used in certain biological applications.

Recently, quantum dots (QDs) derived from two-dimensional (2D) materials, such as graphene quantum dots (GQDs), carbon dots (CDs), polymer dots,¹¹ and black phosphorus (BP)¹² have emerged as superior fluorophores for bio-imaging and optical sensing because of their unique properties, including their tunable photoluminescence (PL), molecular size, excellent photostability, good water solubility, chemical inertness, biocompatibility, ease of functionalization, readiness to be internalized by cells, and low cost. Inspired by the unique 2D characteristics of graphene¹³⁻¹⁴ and black phosphorus,¹⁵ considerable efforts have been devoted to the exploration of new 2D materials. One of the most popular MXene materials, Ti_3C_2 has emerged as the most attractive 2D metal carbides derived from MAX phases. MXene possesses both metallic conductivity and hydrophilicity; therefore, these surfaces are terminated with hydrophilic groups which provide intercalation or surface redox capacitances with superior conductivity ($2400 \text{ S}\cdot\text{cm}^{-1}$, comparable to multilayer graphene).¹⁶ The 2D MXene dots are expected to have good water solubility and have more flexible applications when compared with CDs. Besides, the yields of MXene are high and preparation process is simple and readily scalable when compared with the CD preparation process.¹⁷ Therefore, the luminescent Ti_3C_2 MXene QDs (MQDs) are promising candidate materials for applications involving bioimaging, photocatalysis, biosensors, W-LEDs, and cellular imaging areas. However, the prepared MQDs exhibited excitation-dependent PL spectra with quantum yields of merely 10%, which limits their applications involving the biomedical and optical

fields.¹⁸

Here, we report a high quantum yield (QY) involving MXene quantum dots using a layered Ti_3C_2 nanosheet as a precursor for the preparation of N-doped Ti_3C_2 quantum dots (N-MQDs). The pre-prepared N-MQDs exhibited an excitation-dependent PL spectrum with quantum yields up to 18.7% due to a strong quantum confinement. This is the highest QY reported thus far involving this material.¹⁸⁻²⁰(Table S1). Compared with previous paper, we first proposed the use of heteroatom-doped Ti_3C_2 quantum dots (N-MQDs) to optimize the photoluminescence (PL) properties of MXene quantum dots. To further understand the atomic and electronic mechanism of the N doping effect on the quantum yield of the N-MQDs, well-resolved density functional theoretical (DFT) calculations were employed to investigate the density of the states of both pristine Ti_3C_2 QDs and N-MQDs. what's more, we developed a novel and sensitive biosensor for the detection of Fe^{3+} , leveraging the robust fluorescence properties of the N-MQDs. These results indicated that this material has the potential to act as a fluorescent probe for chemical sensing. In addition, we discovered that N-MQDs are a promising mediator-free biosensor for the detection of H_2O_2 with a high sensitivity, indicating that this material has a great potential for applications involving biological sensing.

2 EXPERIMENTAL SECTION

2.1 Synthesis of N- Ti_3C_2 MXene

Ti_3AlC_2 powder was prepared by ball-milling Ti_2AlC (>92 wt%, 3-ONE-2, Voorhees, NJ) and TiC (99%, Johnson Matthey Electronic, NY) in a 1:1 molar ratio for 24 h using zirconia balls. The mixture was heated to 1350°C for 2 h under argon. The resulting material was crushed using a mortar and pestle. A measured amount of 10 g of the resulting powder was immersed in ≈ 100 mL of a 50% concentrated HF solution (Fisher Scientific, Fair Lawn, NJ)

at room temperature for 2 h. The resulting suspension was then washed several times using deionized water and centrifuged to separate the powders. In some cases, the treated powders were cold pressed at a load corresponding to a pressure of 1 GPa in a freeze dryer to align the flakes.

2.2 Synthesis of N-Ti₃C₂ Quantum Dots

In a typical procedure, 200 mg of Ti₃C₂ MXene was suspended in concentrated nitric acid in an oil bath and held to a constant temperature of 100°C for 24 h. The solution was cooled to room temperature and poured into a beaker containing 100 mL of ice, and NaOH was added until the pH was 7. Nitrogen-doped Ti₃C₂ quantum dots (N-MQDs) were synthesized using the following hydrothermal method. Briefly, a solution of 20 mL of the Ti₃C₂ quantum dots and ethanediamine (2 mL) were added to a 50 mL Teflon-lined, stainless-steel autoclave. Then, the autoclave was kept at a temperature of 160°C for 12 h. The reaction mixture was adequately separated and purified using following procedures. The mixture was filtered through a 0.45 µm polytetrafluoroethylene membrane, and the filtrate was dialyzed in a 1,000 Da dialysis bag for 2 days to obtain the final N-MQDs. The products were filtered first to remove impurities. Then, the product solution was further purified for several days using a dialysis membrane against ultrapure water which was renewed every 10-12 h, until no Na⁺ was detected in the ultrapure water.

2.3 Characterization

The structure of the materials was investigated by X-ray diffraction analysis (XRD, Rigaku D/max-2500PC, Germany) at 40 kV and 100 mA using Cu K α radiation and was performed in an angle range of 5-90°. The GIXRD measurements were performed at the BL14B1 beamline of Shanghai Synchrotron Radiation Facility (SSRF) using X-ray with a wavelength of 0.6887 Å. A ThermoFisher Escalab 250Xi X-ray powder photoelectron spectrometer was

used to analyze the X-ray photoelectron spectroscopy (XPS) of the sample surface composition using an Al K α radiation source with a scattering of 0-5,000 eV. The binding energy was calibrated using the C1s peak contaminate carbon (BE=284.6 eV) as an internal standard. The surface morphology of the materials was characterized with scanning electron microscopy (SEM) using a Hitachi SU8010 with an acceleration voltage of 15 kV. Fourier transform infrared spectroscopy (FTIR, Bruker 70V, USA) was used to characterize the functional groups on the surface before and after the Ti₃C₂ was calcined. The ultraviolet-visible (UV-Vis) absorption spectra of the samples were measured using a UV-Vis spectrometer (Jasco V-570). The obtained PL decay curves were fitted using a single-exponential function: $R(t)=B1 \times e^{-t/\tau}$, where the fit parameter τ is the PL decay time. The systematic error was approximately ± 0.1 ns for all lifetime measurements. Fluorescence measurements were performed with a fluorescence spectrophotometer (FS5 from Techcomp (China) LTD), and the quantum yield (QY) was measured using a FS-30 quantum yield accessory with an integrating sphere. Each measurement was conducted three times to obtain an average value. Scanning transmission electron microscopy (STEM) images and energy-dispersive X-ray spectroscopy (EDS) mapping profiles were collected on a FEI Talos F200X transmission electron microscope operated at 200 kV. The morphology and lattice fringes of the materials were investigated using transmission electron microscopy (TEM) and HRTEM (Model JEM-2100) operated at 200 kV.

2.4 Fe³⁺ detection

In a typical experiment, 3.0 mL of N-Ti₃C₂ quantum dots were diluted to 100 mL with deionized water, and then the fluorescence intensity at 447 nm of N-MQDs (excited by the light at 360 nm) was measured and recorded as the initial fluorescence intensity (F₀). Subsequently, various concentrations of Fe³⁺ were introduced into the above solution. The

fluorescence intensity was measured after 5 min, and this was recorded as the fluorescence intensity for the ending point (F_t). The change in fluorescence intensity (ΔF) is defined as the difference between F_0 and F_t ($\Delta F = F_0 - F_t$).

2.5 Computational Method

In the work, the rigorous ab initio calculations was performed by the Vienna ab initio simulation package (VASP)²¹ based on density functional theory (DFT) and plane-wave basis pseudopotential method. The Perdew-Burke-Ernzerhof (PBE) with generalized gradient approximation (GGA)²² was used here. The cutoff energy of atomic wave functions was 400 eV. The Brillion zone was integrated using Monkhorst-Pack generated sets of k-points²³ with $4 \times 4 \times 4$ used for k-point sampling. In order to elucidate how the presence of the nitrogen (N) defect changes free carrier lifetimes and charge recombination rates, the diagram of the energy levels and charge-transfer processes is plot as shown in Figure. S1.

3 RESULTS AND DISCUSSION

The synthesis scheme of the N-MQDs is manifested in **Figure 1a**. Scanning electron microscopy (SEM) image of the Ti_3C_2 powders obtained after HF etching is shown in **Figure S2**. This shows that the removal of the Al layer from Ti_3AlC_2 resulted in the formation of stacks of Ti_3C_2 nanosheets, which is similar to the production of graphene using graphite exfoliation. The microstructure and corresponding element maps of the prepared Ti_3C_2 was further investigated by scanning transmission electron microscopy (STEM). Figure 1b demonstrates that the Al-layers in Ti_3AlC_2 were successfully removed by the HF solution to form a layered Ti_3C_2 nanostructure. Lattice fringes with an inner-plane spacing at 0.216 nm were depicted, which correspond to the (1 0 5) facet of Ti_3C_2 MXene. The elements Ti and C were uniformly distributed within the layered material (**Figure S3**, Support Information). The stronger carbon signal at the edges of the particle was caused by the conductive paste. Ti_3C_2

was suspended in concentrated sulphuric acid in an oil bath at 100°C for 24 h, and the morphology was investigated using transmission electron microscopy (TEM). The TEM and high-resolution TEM (HRTEM) images (**Figure S4**) sufficiently indicated a clear 2D layered structure of the Ti_3C_2 after undergoing acid treatment.

A representative TEM image of the freshly obtained N-MQDs has been studied. The TEM image of acquired N-MQDs (160°C) and the diameter size distribution (**Figure 1c**) of N-MQDs (160°C) unambiguously illustrate the formation of uniform ultra-small quantum dots with widths ranging from 2 to 7 nm. **Figure 1d** shows clear fringes in each nanocrystal, indicating the single-crystalline feature of the obtained N-MQDs (160°C) sheets. The distance between adjacent lattice fringes was measured to be 0.162 nm, matching with the (1 0 9) lattice of an individual Ti_3C_2 layer. As expected, the N-MQDs formed after the hydrothermal treatment had good solubility in ethanol and water. The average lateral particle sizes were 3.93, 3.7, and 5.76 nm for N-MQDs hydrothermally treated at 120°C, 160°C, and 200°C, respectively (**Figure S5**, Supporting Information). The size distribution was calculated by counting 200 particles, and the lateral sizes of the QDs were directly measured from the TEM images.

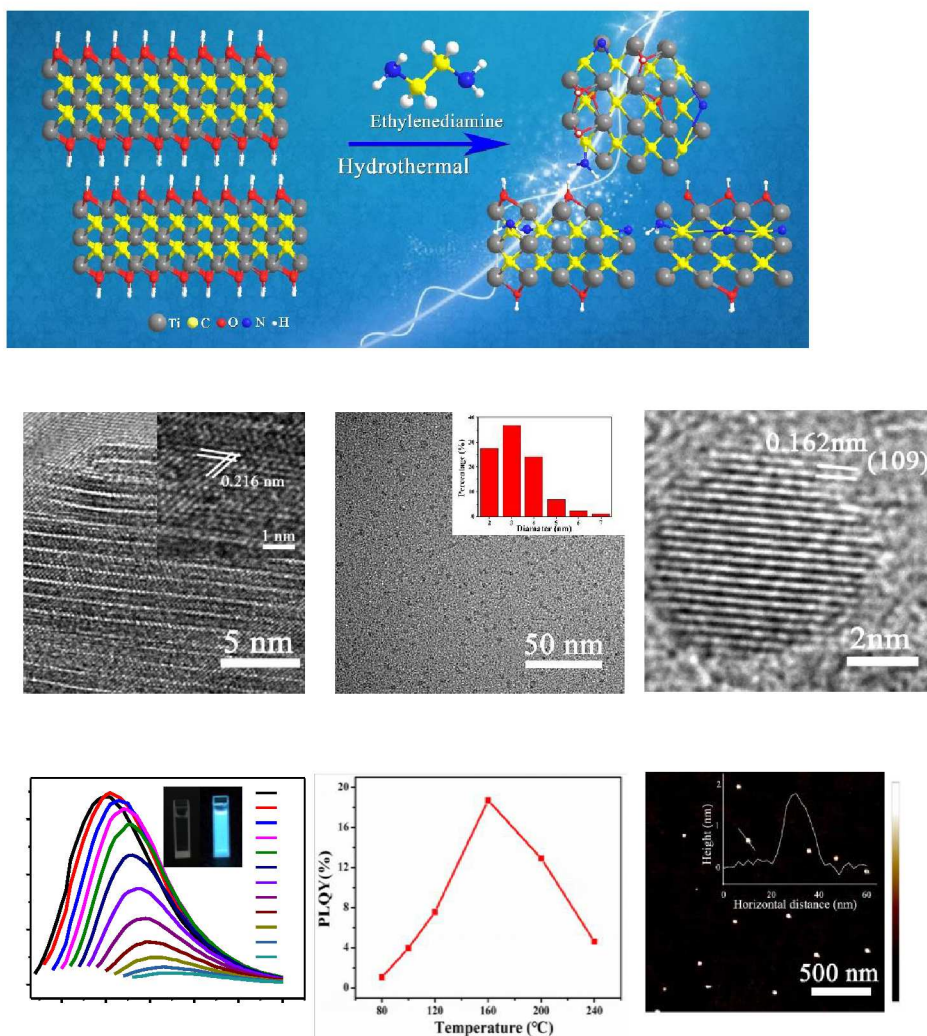


Figure 1. (a) Schematic diagram of the preparation of N-MQDs. (b) HRTEM image of Ti_3C_2 MXene. Inset (top-right): enlarged view of the HRTEM image. (c,d) TEM and HRTEM images of N-MQDs (160°C). Inset (top-right) in (c): diameter size distribution of N-MQDs (160°C). (e) Fluorescent emission spectra of the prepared N-MQDs (160°C) at different excitation wavelengths. Inset (top-right): photographs under UV light (365 nm); (f) PLQY of N-MQDs as a function of hydrothermal reaction temperature. (g) AFM image of the prepared N-MQDs (160°C). Inset (top-right): thickness of the N-MQDs (160°C).

Figure 1e shows the variation of the emission spectra of N-MQDs, excited by light with different wavelengths. The prepared N-MQDs demonstrated a strong emission centered at 447 nm (λ_{em}) when excited at 360 nm (λ_{ex}). The variation in λ_{ex} from 360 nm to 470 nm for N-MQDs only resulted in an intensity decrease of λ_{em} and no change in the peak position, indicating excitation-dependent emission properties of the N-MQDs. The dispersed N-MQDs appeared transparent to the naked eye but emitted a strong blue fluorescence when excited using 365 nm UV radiation (inset of **Figure 1e**). The PLQY of the N-MQDs was influenced by reaction temperature, so the temperature of hydrothermal method was optimized. The result exemplified in **Figure 1f** clearly suggests that PLQY increased gradually up to a maximum value (18.7%) as the temperature increased to 160°C. The facile MXene size and efficient N doping occur to generate MQDs with robust photoluminescence and the highest PLQY of 18.7% at a hydrothermal temperature of 160°C. This is the highest quantum yield reported so far using this material. **Figure 1g** and **Figure S6a-c** delineate the AFM images of different hydrothermal treatment temperatures of N-MQDs, which provide a relatively precise thickness. The thickness distributions indicate that the average thicknesses of the N-MQDs hydrothermally treated at 120°C, 160°C, and 200°C were 0.7, 1.4, and 3.8 nm, respectively. This revealed that most of the N-MQDs treated at 120°C corresponded to monolayer QDs.¹⁸ The N-MQDs treated at 160°C corresponded to bilayers, and the N-MQDs treated at 200°C corresponded to multiple-layers (**Figures S6 and S7**, Supporting Information).

The composition and overall crystallinity of the pristine Ti_3C_2 , Ti_3AlC_2 and N-MQDs were investigated via X-ray diffraction (XRD) (**Figure S8a**). The diffraction of the HF-etched Ti_3C_2 nanosheets presented evident (002) and (004) peaks, which agree with the previous XRD results.²⁴⁻²⁵ This indicates the prepared materials had a 2D layered structure, consistent with our HRTEM and AFM images (**Figures 1d and 1g**). The pattern of the prepared

N-MQDs treated at 160°C unambiguously demonstrated that a 2D layered structure was maintained. The (109) peak of N-MQDs was observed at 56.4°, which was in accordance with the results of TEM image (**Figure 1d**). **Figure S8b** shows the normalized grazing incidence XRD (GIXRD) patterns of N-MQDs and the (002) peak of the N-MQDs presented a slight shift due to nitrogen doping. It is apparent that the (002) peak located at 8.4° for the N-MQDs noticeably shifts to lower angles compared to the (002) peak of the pristine Ti₃C₂ (8.8°). This shift corresponds to an increase in the d-spacing from 1.01 nm to 1.05 nm (Δ d-spacing: ~0.04 nm).

X-ray photoelectron spectroscopy (XPS) was used to determine the nature of chemical bonding in the C 1s, N 1s and Ti 2p region for Ti₃C₂ (**Figures 2a-c and S9**). The C1s XPS spectra of Ti₃C₂ showed four peaks at 281.5, 284.8, 286.2 and 288.6 eV. These spectra (**Figure S9b**, Supporting Information), corresponded to C–Ti, C–C/C–H, C–O and C=O bonds, respectively.²⁶ A peak at 285.7 eV was observed in N-MQDs treated at 120°C and it was attributed to a C–N–H bonding configuration. Another two emerging peaks at 286.1 eV (C=N bonding) and 287.5 eV (C–N bonding) were found in N-MQDs treated at 160°C and 200°C, suggesting that chemical bonds were formed between doped nitrogen atoms and carbon atoms after the N-MQDs underwent hydrothermal treatment. The C1s XPS spectra concerning N-MQDs hydrothermally treated at 120°C, 160°C, and 200°C are shown in **Figure S9b**. C–C/C=O bonds were formed at 120°C, while C–N/C=N bonds tended to form at the higher temperature treatments of 160°C and 200°C. When the N-MQDs were hydrothermally treated at 200°C, the formation of C=N bonds was more dominant, which implied that the formation of C=N may need higher temperature to overcome the energy barrier.

Simultaneously, the bonding configurations of nitrogen atoms in pristine Ti_3C_2 and N-MQDs were characterized using high-resolution N1s spectra. There was no signal intensity in the N1s spectra of pristine Ti_3C_2 . However, four new peaks obtained by peak fitting formed at 397.9, 399.5, 400.2 and 401.2 eV. These peaks corresponded to the Ti-N band, pyrrole-like nitrogen (C=N), N-H band, and “graphitic” nitrogen (C-N).²⁷ The N-H band formed at 120°C and disappeared at higher temperature. “Graphitic” nitrogen appeared at 160°C and 200°C. Additionally, the content of “graphitic” nitrogen increased as the annealing temperature increased.²⁸ As pyrrole-like nitrogen was generated, N doping was inclined to occur at the carbon sites with a larger shrinkage of the defect-induced bond and also at the vertex site of a pentagonal ring if it existed.²⁹ Since the lone pair of graphitic nitrogen had less steric hindrance than that of the pyrrole-like nitrogen, the N-MQDs hydrothermally treated at 200°C with a high content of graphitic N (Table S2, 82.8% of graphitic N in N-MQDs at 200°C compared to 45.7% of graphitic N in N-MQDs at 160°C) formed a more packed and regular structure, in agreement with the low thickness and multiple layers found in the AFM results (**Figures S6–S7**). This study leads to a further understanding of the growth mechanisms of MQDs induced by nitrogen doping.

The O1s XPS spectra of layered Ti_3C_2 was fit by three components located at 530.1, 532.2 and 533.5 eV, which were ascribed to Ti–O–Ti (lattice O), Ti–OH and C–O species, respectively (**Figure S9d**).³⁰ The Ti–OH and C–O species at 532.2 and 533.5 eV unambiguously demonstrated the presence of –OH groups on the surface of Ti_3C_2 . Three new peaks were formed at 530.9, 531.7 and 533.0, and corresponded to Ti–O, C–OH and C=O bands, respectively. This is concordant with the formation of pyrrole-like nitrogen in the N1s spectra. The spectra of Ti 2p can be seen in Figure 2c and show four doublets (Ti 2p_{3/2}–Ti 2p_{1/2}) with a fixed area ratio 2:1 and doublet separation of 5.7 eV were found.²³ The Ti 2p_{3/2} components centered at 454.9 and 458.5 eV were assigned to the Ti–C bond and Ti

ions in valence IV (TiO_2).³¹⁻³² What's more, the Ti-N bond in the N1s spectra (**Figure S9c**) is in line with the Ti-N peak centered at 455.5 eV in the Ti2p spectra.³³ There were no significant differences between annealing temperatures in the Ti2p spectra, which indirectly revealed the catalytic role of Ti in N-MQDs. The impacts of the Ti content on the structure and characteristics of N-MQDs are still under investigation in our group.

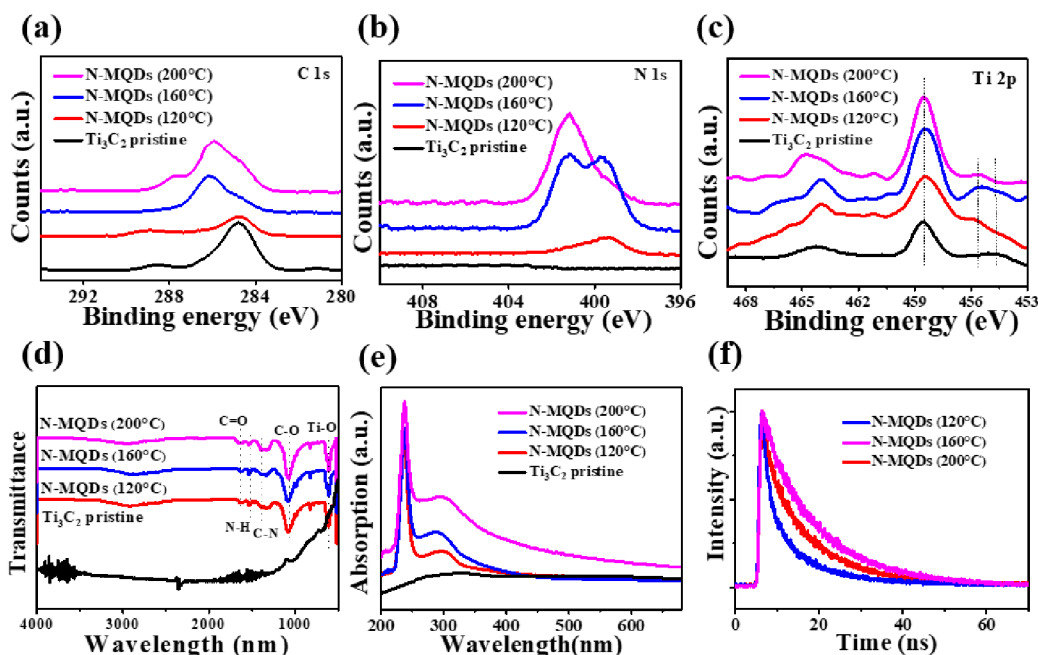


Figure 2. High-resolution XPS spectra of (a) C 1s, (b) N 1s, and (c) Ti 2p for the pristine Ti_3C_2 and N-MQDs. (d) FTIR spectra of the pristine Ti_3C_2 and N-MQDs. (e) UV-vis absorption of the pristine Ti_3C_2 and N-MQDs. (f) Lifetimes of N-MQDs.

The structure and functional groups of N-MQDs were investigated using FTIR (**Figure 2d**). The N-MQDs all manifested identical stretching vibrations. The peak at 1068 cm^{-1} was attributed to C-O bonds. The peak at 1630 cm^{-1} was ascribed to the C=O stretching vibration.³⁴ The N-MQDs were nitrogen doped, so strong peaks around 1531 cm^{-1} and 1378 cm^{-1} were observed, which were assigned to the internal vibration of the N-H bonds and C-N stretching vibrations, respectively. In particular, the vibration of the Ti-O bond may account

for the peak at 615 cm^{-1} .³⁵ **Figure 2e** shows the UV-vis absorption spectra of the pristine Ti_3C_2 MXene and N-MQDs. In the UV-vis absorption spectra of N-MQDs, a typical absorption peak at 236 nm was observed. Besides the strong peak at 236 nm, an absorption band centered at 290 nm in the N-MQDs was also detected. According to first-principles density functional theory (DFT) calculations, these absorption peaks can be attributed to the trapping of excited state energy by the surface states. The UV-Vis and PL spectra of the aqueous dispersion revealed that the prepared QDs had a blue fluorescent color. **Figure 2f** shows that the lifetime of N-MQDs solutions varied with different reaction temperatures. The resultant lifetimes were 5.89, 7.06 and 6.46 ns for N-MQDs hydrothermally treated at 120°C , 160°C and 200°C , respectively. The enhanced lifetime of the N-MQDs hydrothermally treated at 160°C was correlated with the nature of the doped nitro-gen at that corresponding temperature.

To further understand the atomic and electronic mechanism of the N doping effect on the quantum yield of the N-MQDs, well-resolved DFT calculations were employed to investigate the density of the states of both pristine Ti_3C_2 QDs (MQDs) and N-MQDs. Ti_3C_2 always terminates functional groups including F, OH and O. F and OH groups can be removed using a physical or chemical approach.³⁶ Thus, Ti_3C_2 terminated with an O group was used for DFT calculations in this work. The total and projected density of the states of $\text{Ti}_3\text{C}_2\text{O}_2$ QDs and $\text{Ti}_3\text{C}_{2-x}\text{N}_x\text{O}_2$ QDs are depicted in **Figure 3**. For pristine MQDs, as shown in Fig. 3 (a), there are energy gap and sub-gap (0.15 eV), while, for N-MQDs, the gap is becoming broad, and federating gasp states in sub-gap. Considering the mechanism of carrier-life in Fig. S1, once can know that, N-QMDs is good for reduction chare and energy loss resulting improving PLYQ, which is in consonance with results reported by Anasori et al.³⁷ **Figure 3b** displays that there was a chemical bond between Ti and N in $\text{Ti}_3\text{C}_{2-x}\text{N}_x\text{O}_2$ QDs. There were prominent gap states, which increased the lifetime of the carrier and improved quantum yields. This

result was in agreement with our experimental results which revealed a lifetime increase from 5.89 ns to 7.06 ns (**Figure 2f**). A comparison between the MQDs and N-MQDs (**Figure 3**) reveals that the energy gap was widened because of nitrogen doping, which increased the lifetime of the carrier and improved quantum yields. Moreover, the N impurities introduced gap states closing to LUMO in N-MQDs, which was desirable for rapid electron migration and resulted in an increased carrier lifetime. The work function of MQDs and N-MQDs was calculated (**Figure S10**). Interestingly, the work function of N-MQDs was smaller than that of the MQDs, which suggested that electron migration was relatively easier in N-MQDs than pristine MQDs.

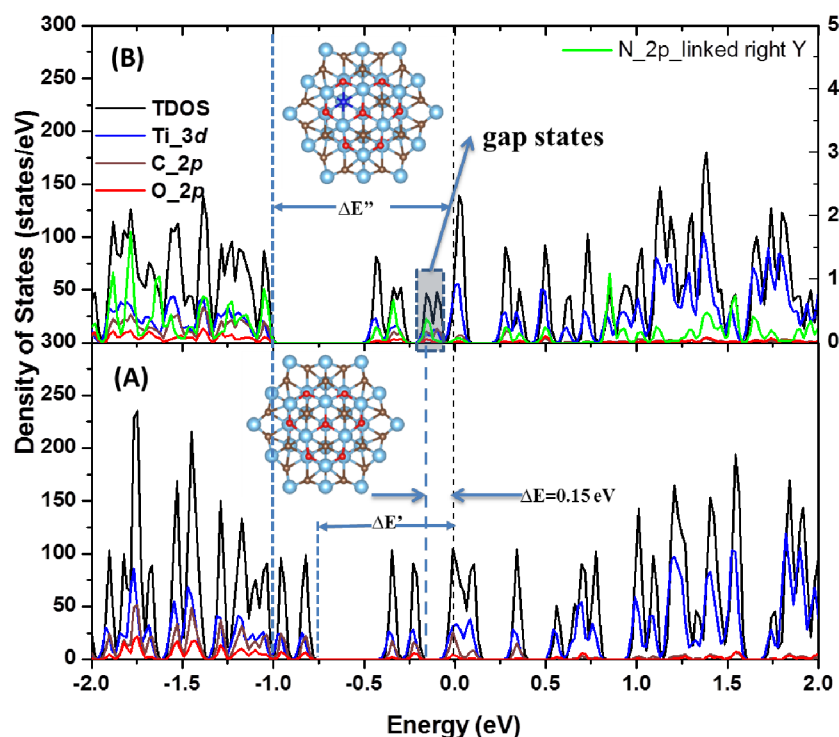


Figure 3. DFT calculated total and projected density of states of (a) $\text{Ti}_3\text{C}_2\text{O}_2$ QDs and (b) $\text{Ti}_3\text{C}_{2-x}\text{N}_x\text{O}_2$ QDs

The photoluminescence spectra (UV light 360 nm) of ethanediamine and Ti_3C_2 (without acid treatment) after undergoing the hydro-thermal reaction at 160°C for 12h is presented in

Figure S11. The ethanediamine and Ti_3C_2 showed no emission intensity. The life-times of the N-MQDs were influenced by the reaction temperature. The hydrothermal treatment temperatures investigated in this study were 80, 100, 120 and 200°C. **Figure S12** illustrates that the life-times increased gradually up to maximum values of 7.06 ns as the temperature was increased to 160°C, followed by a decrease upon further increasing the temperature, which may be due a chemical state change.

Stabilizing the fluorescence of N-MQDs over a wide range of pH values can reveal their feasibility for use in a variety of applications. Hence, the influence of different pH values on the fluorescence intensity of N-MQDs was evaluated. **Figure S13** shows the fluorescent intensity at 447 nm under 360 nm light excitation with various pH levels. A gradual increase in intensity was observed up to pH 3, after which the N-MQDs demonstrated a steady and strong fluorescence (from 3.0 to 12.0). The wide range of fluorescence demonstrates that the N-MQDs are a promising candidate for use in biological applications. To further verify the stability of N-MQDs, the PL intensities and absorption over different lengths of time were investigated (**Figure S14**). There were no identifiable changes in the PL intensities and absorption over the various lengths of time, indicating sufficient surface passivation of the N-MQDs.

Based on the excellent PLQY properties of N-MQDs, we explored their potential for environmental and/or biomedical applications. The particular application involved adopting N-MQDs as probes for the detection of Fe^{3+} . The conventional technologies for Fe^{3+} detection include ultraviolet-visible spectrometry (UV-Vis) and inductively coupled plasma mass spectrometry (ICP-MS). However, these detection methods, especially ICP-MS, require expensive equipment operated by a professional technician. Fluorescence-based technologies, on the other hand, can be employed for Fe^{3+} detection with increased sensitivity, a fast

response, and easy operation. In our study, the strong emission of N-MQDs at 447 nm was used for the ultra-trace detection of Fe^{3+} . The prepared N-MQDs exhibited excellent efficiency for detecting Fe^{3+} , and a significant decrease (near quenching) in intensity was observed upon the addition of 1000 μM of Fe^{3+} (**Figure 4a**). The quenching of fluorescence by Fe^{3+} was attributed to its ability to facilitate the electron/hole recombination annihilation through an alternate and efficient electron transfer process. Moreover, after the abrupt changes observed upon addition of Fe^{3+} , only inconspicuous changes were observed after 0.5 min. Thus, 0.5 min was defined as the detection time in the experiment for the detection of Fe^{3+} . **Figure 4b** illustrates the change in the fluorescence intensity of N-MQDs in the presence of increasing concentrations of Fe^{3+} . Each spectrum was recorded after 5 min of equilibration time. A linear relationship was observed between the Fe^{3+} concentration and fluorescence intensity. The resultant calibration curve for Fe^{3+} corroborated excellent linearity with the concentration in the range from 2 to 5000 μM with a coefficient of determination of 0.9281 (**Figure 4c**). The detection limit was as low as 2 μM , which compares well with previous reports for Fe^{3+} detection.³⁸ In combination with the fast and ultra-low detection limit, for practical applications, the selectivity of the process is also critical. To evaluate the selectivity of the proposed Fe^{3+} sensor, 5 mM of various metal ions, including Na^+ , Mg^{2+} , Cu^{2+} , K^+ , Fe^{3+} , Mn^{2+} , Zn^{2+} , Ca^{2+} , Al^{3+} , Ce^{3+} , Cu^+ and Ni^{2+} were added to the N-MQDs solution in addition to Fe^{3+} . The change in fluorescence intensity (ΔF) at 447 nm was recorded for each of these interference ions. As demonstrated in **Figure 4d**, substantial quenching of the fluorescence of N-MQDs was only observed upon addition of Fe^{3+} , while the influence of other metal ions on N-MQDs fluorescence quenching was almost negligible. Moreover, the changes of lifetime (**Figure 4e**) and absorption (**Figure 4f**) provided evidence that the change of the surface state of the N-MQDs resulted from Fe^{3+} . There was a complexation effect as Fe^{3+} was introduced, causing the electron or energy

transfer. Thus, the N-MQDs were found to have a good specificity and selectivity for the detection of Fe^{3+} . This confers the significant contributions on the emerging roles of N-MQDs in protecting and monitoring the environment.

The possibility of detecting H_2O_2 with the aid of Fe^{2+} was also investigated. Time-dependent changes in the fluorescence intensity of N-MQDs in the presence of $50 \mu\text{M}$ H_2O_2 solution was examined (**Figure S15a**). No observable change was noted, implying that the fluorescence of N- Ti_3C_2 quantum dots could not be quenched by H_2O_2 alone. A similar study in the presence of $50 \mu\text{M}$ Fe^{2+} alone was carried out (**Figure S15b**), which did not signify any appreciable changes in intensity. However, when H_2O_2 and Fe^{2+} were added simultaneously, the fluorescence intensity of N-MQDs decreased substantially. **Figure S15c** indicates the change of fluorescent intensity (ΔF) of the N-MQDs in the presence of both H_2O_2 and Fe^{2+} . After 10 min, the fluorescence intensity decreased up to 69.78%. This demonstrates the feasibility of using N-MQDs as a fluorescent probe for H_2O_2 detection. The results prove that the obtained N-MQDs are an ideal bio-probe for sensitive and fast detection of H_2O_2 , which can be adapted for monitoring cell health and biology sensing applications.³⁹

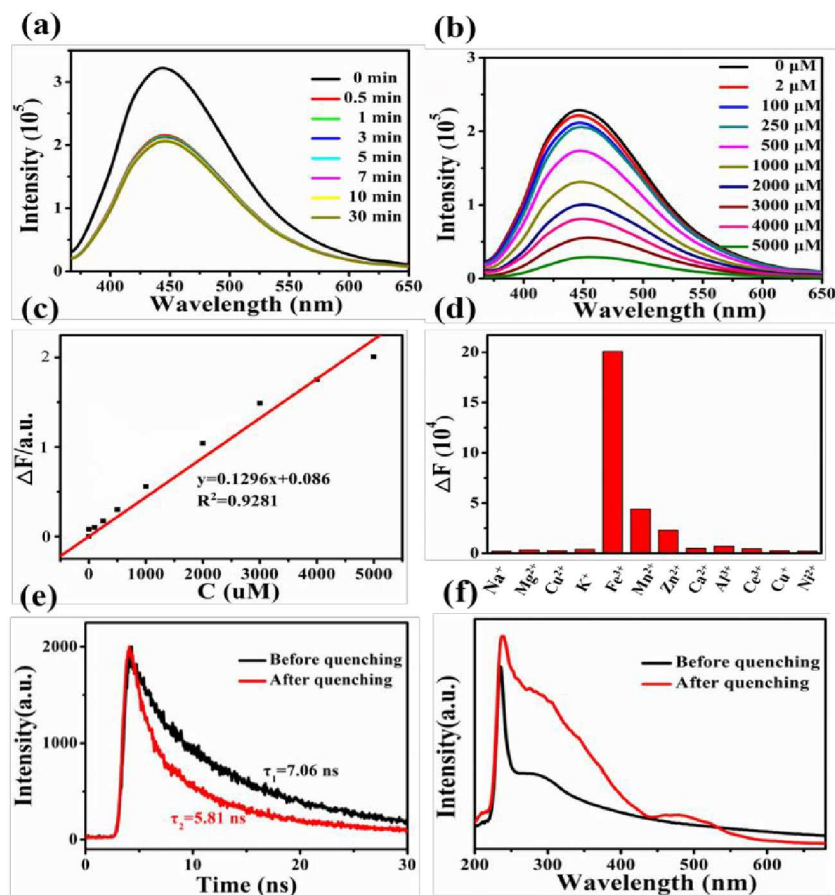


Figure 4. (a) Time-dependent fluorescence changes of N-MQDs in the presence of Fe³⁺ (1000 μM). (b) PL emission spectra of the N-MQDs solution with different concentrations of Fe³⁺. (c) ΔF calibration curve of N-MQDs solution versus the concentration of Fe³⁺. (d) The change of fluorescent intensity in 447nm for N-MQDs in the presence of various metal ions. (e) Lifetimes and (f) absorption spectra before and after the quenching of N-MQDs by Fe³⁺.

4 CONCLUSIONS

In summary, novel photoluminescent N-MQDs were developed using a layered Ti₃C₂ nanosheet as the starting material and ethylenediamine as a nitrogen source. The chemical structure and PL mechanism of the N-MQDs prepared at different temperatures were

investigated. The obtained N-MQDs exhibited an excellent blue luminescence (emission at 447 nm) and a PLQY of up to 18.7%, which was the highest ever reported in literature. In particular, N-MQDs were found to be very suitable for detecting Fe^{3+} ions with high selectivity. The use of N-MQDs as an efficient fluorescence probe for the detection of H_2O_2 was also confirmed. The Fenton reaction-based mechanism was used for the detection. As such, the novel N-MQDs will open up more applications in the field of electronics, solar cells, sensing and bio-imaging.

Supporting Information.

SEM image of the pristine Ti_3C_2 , XRD spectra of N-MQDs, pristine Ti_3C_2 and Ti_3AlC_2 , TEM-EDS elemental mapping images of the pristine Ti_3C_2 sheet, Diameter size distribution of N-MQDs of different hydrothermal temperature treatments, Thickness distribution of the prepared N-MQDs, AFM image of the prepared N-MQDs, High-resolution XPS spectra for pristine Ti_3C_2 and N-MQDs. (b-d) C1s, N1s, and O1s XPS spectra for pristine Ti_3C_2 and N-MQDs, Photoluminescence spectrum of the N-MQDs treated at different hydrothermal reaction temperatures, Lifetime of N-MQDs as a function of hydrothermal reaction temperature, The fluorescence intensity of N-MQDs at 447 nm excited at 360 nm as a function of pH, Time-dependent fluorescence intensity and absorption changes of the N-MQDs (160°C), Time-dependent fluorescence intensity of N-MQDs (Figures S1-14).

This material is available free of charge via the Internet at <http://pubs.acs.org>.

AUTHOR INFORMATION

Corresponding Author

* Address correspondence to: xuquan@cup.edu.cn, lineng@whut.edu.cn

Conflict of Interest

The authors declare no conflict of interest.

ACKNOWLEDGMENT

Quan Xu would like to thank the Beijing Nova Program Interdisciplinary Studies Cooperative project (No. Z181100006218138), Science Foundation of China University of Petroleum-Beijing (No. 2462018BJC004) for the support. Neng Li would like to thank the National Natural Science Foundation of China (No. 11604249), the Fundamental Research Funds for the Central Universities, the research board of the State Key Laboratory of Silicate Materials for Architecture. Aiguo Zhou would like to thank the National Natural Science Foundation of China (No. 51772077; 51472075). This material is also supported by the National Institute of Food and Agriculture, U.S. Department of Agriculture, and McIntire Stennis under accession number 1009735. We are grateful to the Shanghai Supercomputer Center for providing computing resources.

REFERENCES:

- (1) Barsoum, M. W., The $M_{N+1}A_XN$ phases: A new class of solids: Thermodynamically stable nanolaminates. *Prog. Solid. State. Ch.* **2000**, *28*, 201-281.
- (2) Chen, X.; Kong, Z.; Li, N.; Zhao, X.; Sun, C., Proposing the pro-spects of Ti_3CN transition metal carbides (MXenes) as anodes of Li-ion batteries: a DFT study. *Phys. Chem. Chem. Phys.* **2016**, *18*, 32937-32943.
- (3) Naguib, M.; Mochalin, V. N.; Barsoum, M. W.; Gogotsi, Y., 25th anniversary article: MXenes: a new family of two-materials. *Adv. Mater.* **2014**, *26*, 992.
- (4) Mashtalir, O.; Cook, K. M.; Mochalin, V. N.; Crowe, M.; Bar-soum, M. W.; Gogotsi, Y., Dye adsorption and decomposition on two-dimensional titanium carbide in aqueous media. *J. Mater. Chem. A.* **2014**, *2*, 14334-14338.
- (5) Ran, J.; Gao, G.; Li, F. T.; Ma, T. Y.; Du, A.; Qiao, S. Z., Ti_3C_2 MXene co-catalyst on metal sulfide photo-absorbers for enhanced visible-light photocatalytic hydrogen production. *Nat. Commun.* **2017**, *8*, 13907.

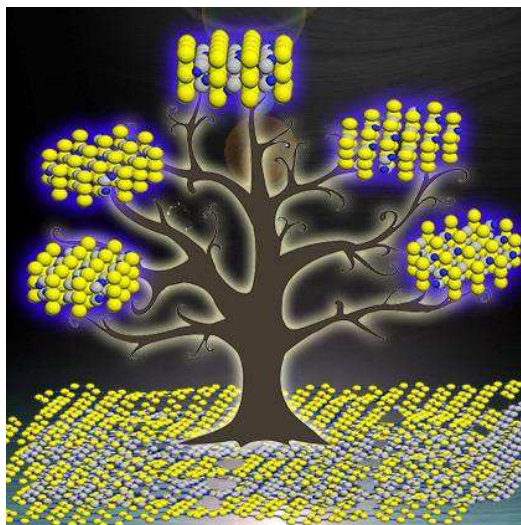
- (6) Li, N.; Chen, X.; Ong, W. J.; MacFarlane, D. R.; Zhao, X.; Cheetham, A. K.; Sun, C., Understanding of electrochemical mechanisms for CO₂ capture and conversion into hydrocarbon fuels in transition-metal carbides (MXenes). *ACS Nano* **2017**, *11*, 10825-10833.
- (7) Hu, M.; Li, Z.; Tao, H.; Zhu, S.; Chao, Z.; Wang, X., High-Capacitance Mechanism for Ti₃C₂T_x MXene by in Situ Electrochemical Raman Spectroscopy Investigation. *ACS Nano* **2016**, *10*, 11344-11350.
- (8) Lukatskaya, M. R.; Bak, S. M.; Yu, X.; Yang, X. Q.; Barsoum, M. W.; Gogotsi, Y., Probing the mechanism of high capacitance in 2D titanium carbide using in situ X-ray absorption spectroscopy. *Adv. Energy Mater.* **2015**, *5*, 1500589.
- (9) Han, M.; Yin, X.; Wu, H.; Hou, Z.; Song, C.; Li, X.; Zhang, L.; Cheng, L., Ti₃C₂ MXenes with modified surface for high-performance electromagnetic absorption and shielding in the X-band. *ACS Appl. Mater. Inter* **2016**, *8*, 21011-21019
- (10) Ghidui, M.; Halim, J.; Kota, S.; Bish, D.; Gogotsi, Y.; Barsoum, M. W., Ion-exchange and cation solvation reactions in Ti₃C₂ MXene. *Chem. Mater.* **2016**, *28*, 3507-3514.
- (11) Ritter, K. A.; Lyding, J. W., The influence of edge structure on the electronic properties of graphene quantum dots and nanoribbons. *Nat. Mater.* **2009**, *8*, 235-242.
- (12) Pengfei, C.; Neng, L.; Xingzhu, C.; Wee-Jun, O.; Xiujian, Z., The rising star of 2D black phosphorus beyond graphene: synthesis, properties and electronic applications. *2D Mater.* **2018**, *5*, 014002.
- (13) Wurm, J.; Rycerz, A.; Adagideli, I.; Wimmer, M.; Richter, K.; Baranger, H. U., Symmetry classes in graphene quantum dots: Universal spectral statistics, weak localization, and conductance fluctuations. *Phys. Rev. Lett.* **2009**, *102*, 056806.
- (14) Bcm, M.; Gam, H.; Caputo, C. A.; Prantl, S.; Godin, R.; Durrant, J. R.; Reisner, E., Enhancing Light Absorption and Charge Transfer Efficiency in Carbon Dots through Graphitization and Core Nitrogen Doping. *Angew. Chem. Int. Ed.* **2017**, *56*, 6459.
- (15) Zhang, X.; Xie, H.; Liu, Z.; Tan, C.; Luo, Z.; Li, H.; Lin, J.; Sun, L.; Chen, W.; Xu, Z., Black phosphorus quantum dots. *Angew. Chem. Int. Ed.* **2015**, *54*, 3653-3657.
- (16) Xue, Q.; Zhang, H.; Zhu, M.; Pei, Z.; Li, H.; Wang, Z.; Huang, Y.; Deng, Q.; Zhou, J., Photoluminescent Ti₃C₂ MXene Quantum Dots for Multicolor Cellular Imaging. *Adv. Mater.* **2017**, *29*, 1604847.

- (17) Naguib, M.; Mochalin, V. N.; Barsoum, M. W.; Gogotsi, Y., 25th anniversary article: MXenes: a new family of two-dimensional materials. *Adv. Mater.* **2014**, *26*, 992-1005.
- (18) Xue, Q.; Zhang, H.; Zhu, M.; Pei, Z.; Li, H.; Wang, Z.; Huang, Y.; Deng, Q.; Zhou, J. Photoluminescent Ti_3C_2 MXene Quantum Dots for Multicolor Cellular Imaging. *Adv. Mater.* **2017**, *29*, 1604847.
- (19) Chen, X.; Sun, X. K.; Xu, W.; Pan, G. C.; Zhou, D. L.; Zhu, J. Y.; Wang, H.; Bai, X.; Dong, B.; Song, H. W., Ratiometric photoluminescence sensing based on Ti_3C_2 MXene quantum dots as an intra-cellular pH sensor. *Nanoscale* **2018**, *10*, 1111-1118.
- (20) Lin, H. H.; Wang, C. X.; Wu, J. P.; Xu, Z. Z.; Huang, Y. J.; Zhang, C., Colloidal synthesis of MoS_2 quantum dots: size-dependent tunable photoluminescence and bioimaging. *New J. Chem.* **2015**, *39*, 8492-8497.
- (21) Kresse, G.; Furthmüller, J., Efficient iterative schemes for ab initio total-energy calculations using a plane-wave basis set. *Comp. Mater. Sci.* **1996**, *6*, 15-50.
- (22) Perdew, J. P.; Chevary, J. A.; Vosko, S. H.; Jackson, K. A.; Pederson, M. R.; Singh, D. J.; Fiolhais, C., Atoms, molecules, solids, and surfaces: Applications of the generalized gradient approximation for exchange and correlation. *Phys. Rev. B* **1992**, *46*, 6671-6686.
- (23) Monkhorst, H. J.; Pack, J. D., Special points for Brillouin-zone integrations. *Phys. Rev. B* **1976**, *13*, 5188-5192.
- (24) Zhu, J.; Tang, Y.; Yang, C.; Wang, F.; Cao, M. Composites of TiO_2 nanoparticles deposited on Ti_3C_2 MXene nanosheets with enhanced electrochemical performance. *J. Electrochem. Soc.* **2016**, *163*, 785-791.
- (25) Tang, Y.; Zhu, J.; Yang, C.; Wang, F., Enhanced supercapacitive performance of manganese oxides doped two-dimensional titanium carbide nanocomposite in alkaline electrolyte. *J. Alloys Compd.* **2016**, *685*, 194-201.
- (26) Rakhi, R. B.; Ahmed, B.; Hedhili, M. N.; Anjum, D. H.; Al-shareef, H. N., Effect of Postetch Annealing Gas Composition on the Structural and Electrochemical Properties of Ti_2CT_x MXene Electrodes for Supercapacitor Applications. *Chem. Mater.* **2015**, *27*, 5314-5323.
- (27) Liu, X.; Dai, L., Carbon-based metal-free catalysts. *Nat. Rev. Mater.* **2016**, *1*, 16064.

- (28) Sheng, Z. H.; Shao, L.; Chen, J. J.; Bao, W. J.; Wang, F. B.; Xia, X. H., Catalyst-Free Synthesis of Nitrogen-Doped Graphene via Thermal Annealing Graphite Oxide with Melamine and Its Excellent Electrocatalysis. *Acs Nano* **2011**, *5*, 4350-4358.
- (29) Hou, Z.; Wang, X.; Ikeda, T.; Terakura, K.; Oshima, M.; Ka-kimoto, M.-a.; Miyata, S., Interplay between nitrogen dopants and native point defects in graphene. *Physics* **2012**, *85*, 2207-2211.
- (30) Li, B.; Zhao, Z.; Gao, F.; Wang, X.; Qiu, J., Mesoporous micro-spheres composed of carbon-coated TiO₂ nanocrystals with ex-posed {0 0 1} facets for improved visible light photocatalytic activity. *Appl. Catal. B-Environ.* **2014**, *147*, 958-964.
- (31) Yang, H. G.; Sun, C. H.; Qiao, S. Z.; Zou, J.; Liu, G.; Smith, S. C.; Cheng, H. M.; Lu, G. Q., Anatase TiO₂ single crystals with a large percentage of reactive facets. *Nature* **2008**, *453*, 638.
- (32) Dang, B. H. Q.; Rahman, M.; Macelroy, D.; Dowling, D. P., Evaluation of microwave plasma oxidation treatments for the fabrication of photoactive un-doped and carbon-doped TiO₂ coatings. *Anal. Chim. Acta.* **2012**, *206*, 4113-4118.
- (33) Wen, Y. Y.; Rufford, T. E.; Chen, X. Z.; Li, N.; Lyu, M. Q.; Dai, L. M.; Wang, L. Z., Nitrogen-doped Ti₃C₂T_x MXene electrodes for high-performance supercapacitors. *Nano Energy* **2017**, *38*, 368-376.
- (34) Boota, M.; Anasori, B.; Voigt, C.; Zhao, M. Q.; Barsoum, M. W.; Gogotsi, Y., Pseudocapacitive Electrodes Produced by Oxidant-Free Polymerization of Pyrrole between the Layers of 2D Titanium Carbide (MXene). *Adv. Mater.* **2016**, *28*, 1517.
- (35) Luo, J.; Tao, X.; Zhang, J.; Xia, Y.; Huang, H.; Zhang, L.; Gan, Y.; Liang, C.; Zhang, W., Sn⁴⁺ Ion Decorated Highly Conductive Ti₃C₂ MXene: Promising Lithium-Ion Anodes with Enhanced Volumetric Capacity and Cyclic Performance. *ACS Nano* **2016**, *10*, 2491-2499.
- (36) Li, R.; Zhang, L.; Shi, L.; Wang, P., MXene Ti₃C₂: An Effective 2D Light-to-Heat Conversion Material. *ACS Nano* **2017**, *11*, 3752-3759.
- (37) Anasori, B.; Xie, Y.; Beidaghi, M.; Lu, J.; Hosler, B.; Kent, P.; Gogotsi, Y.; Barsoum, M., Two-dimensional, ordered, double transition metals carbides (MXenes). *ACS Nano* **2015**, *9*, 9507-9516.
- (38) Zhu, S.; Meng, Q.; Wang, L.; Zhang, J.; Song, Y.; Jin, H.; Zhang, K.; Sun, H.; Wang, H.; Yang, B., Highly photoluminescent carbon dots for multicolor patterning, sensors, and bioimaging. *Angew. Chem. Int. Ed. Engl.* **2013**, *52*, 3953

- (39) Xu, Q.; Liu, Y.; Su, R.; Cai, L.; Li, B.; Zhang, Y.; Zhang, L.; Wang, Y.; Wang, Y.; Li, N.; Gong, X.; Gu, Z.; Chen, Y.; Tan, Y.; Dong, C.; Sreeprasad, T. S., Highly fluorescent Zn-doped carbon dots as Fenton reaction-based bio-sensors: an integrative experimental-theoretical consideration. *Nanoscale* **2016**, *8*, 17919-17927.

Table of Contents Graphic



High Photoluminescence Quantum Yield of 18.7% by Nitrogen-Doped Ti_3C_2 MXene Quantum Dots